Novel 2D layered g-C_3N_4 nanocomposite materials for sustainable wastewater treatment by catalytic degradation of toxic dye

Khatun, Most Munera
Faculty of Materials Science and Chemistry, China University of Geosciences

Miah, Mohammad Raza
Laboratory of Bio-based Polymeric Materials Technology and Application of Zhejiang Province, Ningbo Institute of Materials Technology and Engineering, Chinese Academy of Sciences

Yan, Chunjie
Faculty of Materials Science and Chemistry, China University of Geosciences

Foijunnesa, Most
College of Chemistry & Chemical Engineering, Wuhan Textile University

他

出版情報：Optik. 311, pp.171959-, 2024-09. Elsevier
バージョン：

Optik - International Journal for Light and Electron Optics 311 (2024) 171959

Contents lists available at ScienceDirect

Optik

journal homepage: www.elsevier.com/locate/ijleo

Original research article

Novel 2D layered g-C_3N_4 nanocomposite materials for sustainable wastewater treatment by catalytic degradation of toxic dye

Most Munera Khatun [a], Mohammad Raza Miah [b,c], Chunjie Yan [a,*], Most Foijunnesa [d], M.Mahbubul Bashar [e], Shahjalal Khandaker [f,g,**], Takahiro Kuba [g], Khalid A. Alzahrani [h,i], M.A. Shenashen [j], Mohammed M. Rahman [h,i], Abdullah M. Asiri [h,i], Aminul Islam [k], Md. Munjur Hasan [l,m], Md. Rabiul Awual [l,n,***]

[a] *Faculty of Materials Science and Chemistry, China University of Geosciences, Lumo Road 388, Wuhan, 430074, P.R. of China*
[b] *Laboratory of Bio-based Polymeric Materials Technology and Application of Zhejiang Province, Ningbo Institute of Materials Technology and Engineering, Chinese Academy of Sciences, Ningbo 315201, P. R. of China*
[c] *University of Chinese Academy of Sciences, Beijing 100049, P. R. of China*
[d] *College of Chemistry & Chemical Engineering, Wuhan Textile University, Wuhan, 430079, P.R. of China*
[e] *Department of Textile Engineering, Mawlana Bhashani Science and Technology University, Santosh, Tangail, 1902, Bangladesh*
[f] *Department of Textile Engineering, Dhaka University of Engineering and Technology, Gazipur, Bangladesh*
[g] *Department of Urban and Environmental Engineering, Graduate School of Engineering, Kyushu University, 744 Motooka, Nishi-ku, Fukuoka, 819-0395, Japan*
[h] *Center of Excellence for Advanced Materials Research, King Abdulaziz University, Jeddah 21589, Saudi Arabia*
[i] *Chemistry Department, Faculty of Science, King Abdulaziz University, Jeddah 21589, Saudi Arabia*
[j] *Department of Chemistry, Faculty of Science, Islamic University of Madinah, Madinah 42351, Saudi Arabia*
[k] *Department of Petroleum and Mining Engineering, Jashore University of Science and Technology, Jashore-7408, Bangladesh*
[l] *Department of Applied Chemistry & Chemical Engineering, University of Dhaka, Dhaka 1000, Bangladesh*
[m] *Department of Chemistry, Graduate School of Science, Osaka University, Osaka 560-0043, Japan*
[n] *Western Australian School of Mines: Minerals, Energy and Chemical Engineering, Curtin University, GPO Box U 1987, Perth, WA, 6845, Australia*

ARTICLE INFO

Keywords:
Photocatalytic degradation
Graphitic carbon nitride (g-C_3N_4)
Nanocomposites
Methylene blue (MB) dye
Wastewater treatment

ABSTRACT

The photocatalytic degradation technique is one of the suitable ways of dealing with environmental pollutant decontamination. This study demonstrates the ability of graphitic carbon nitride (g-C_3N_4) nanocomposites containing tellurium (Te) and molybdenum disulfide (MoS_2) to photocatalytically destroy organic cationic methylene blue (MB) dye, which is primarily used in the textile industry. Using the alkali treatment approach, layered graphitic carbon nitride (g-C_3N_4) was created. Using MoS_2 and Te, several g-C_3N_4 nanocomposites were created using ultrasonic calcination techniques. After the MoS_2 and Te were immobilized individually, the composites underwent a methodical characterization process utilizing a variety of instruments, including XRD and SEM. Using a 2D layered nano-g-C_3N_4 substrate, the photo-catalytic degradation reaction of MB was observed, and a UV spectrophotometer was used to determine the absorbance of the MB dye. Using 0.2 % MoS_2/g-C_3N_4 and 5 % Te/g-C_3N_4, the photocatalytic degradation

* Corresponding author.
** Corresponding author at: Department of Textile Engineering, Dhaka University of Engineering and Technology, Gazipur, Bangladesh.
*** Corresponding author at: Department of Applied Chemistry & Chemical Engineering, University of Dhaka, Dhaka 1000, Bangladesh.
E-mail addresses: chjyan@cug.edu.cn (C. Yan), s.khandaker@duet.ac.bd (S. Khandaker), rabiul.awual@dims-bd.org, rawual76@yahoo.com, rabiul.awual@curtin.edu.au (Md.R. Awual).

https://doi.org/10.1016/j.ijleo.2024.171959
Received 14 January 2024; Received in revised form 28 April 2024; Accepted 11 July 2024
Available online 11 July 2024

efficiency of the MB dye (10, 15, and 20 mg/L) solution was examined. In comparison to other produced nanocomposites, the 5 % Te/g-C_3N_4 composite was shown to have the highest photocatalytic activity in terms of dye degradation ability, and about 100 % of the MB dyes were degraded in less than 60 minutes. As the concentration of MB increased, the dye degradation efficiency of g-C_3N_4 nanocomposites steadily dropped, and the degradation rate of MB was around 1.5 mg/L.

1. Introduction

Photocatalytic materials are primarily semiconductor materials incorporating metal elements [1]. The photocatalytic activity of semiconductor photocatalytic materials can be enhanced by their large surface area and better transmittance efficiency of photo-generated carriers, which can be achieved through two-dimensional (2D) layered structure [2] and nano-scale particle size [3].

In general, graphitic carbon nitride (g-C_3N_4) is an organic non-metal semiconductor with several advantages in an easy preparation procedure and plenty of raw materials [4–6]. In addition to absorbing visible light and having a low bandgap, the g-C_3N_4 has appropriate band positions in the valence band (1.4 eV) and conduction band (-1.3 eV) [7–9]. Water (H_2O) can produce both H_2 and O_2 when the oxidation and reduction layers of g-C_3N_4 are at their absolute values [10]. In order to address the energy crisis, g-C_3N_4 was employed as a viable photo-catalytic hydrogen generation source that can be partially removed by photo-catalytic degradation of pollutants in environmental problems [11–13]. The strong electron-generating potential of the photo-generated holes makes it simple to convert OH^- and H_2O adsorbed on the photocatalyst's surface to hydroxyl radicals (•OH) [14]. Certain organic contaminants are oxidized directly by photo-generated holes when their oxidation potential is greater than the photocatalyst's valence band potential [15]. It is simple to reduce dissolved oxygen in water to superoxide ion radical ($\bullet O_2^-$), hydroperoxide radical ($HO_2\bullet$), hydrogen peroxide (H_2O_2), etc., H_2O_2 further because photogenerated electrons have a strong reducing capacity [16]. Hydroxyl radicals are produced by the process. Active and highly oxidizing free radicals produced during photo-catalysis include superoxide ion radicals, hydro-peroxide radicals, and hydroxyl radicals. These radicals can convert a variety of organic contaminants into carbon dioxide (CO_2) and water (H_2O) [17]. In addition, the endothermic nature of the process of breaking down hydrogen and oxygen results in a typical Gibbs free energy of 238 KJ/mol, or 1.23 eV [18]. Consequently, the photo-catalytic material's bandgap width needs to be larger than 1.23 eV [19]. However, the photo-catalytic material's restricted bandwidth shouldn't be too high to maximize solar energy use. It needs to efficiently absorb a significant amount of solar light that is visible [20]. Moreover, the physical characteristics of bulk and multilayer MoS_2 differ [21]. The prohibited bandwidth increases with decreasing MoS_2 layer count because of the quantum confinement phenomenon [22]. Conduction band potential is more negative and valence band potential is more negative due to an increase in the prohibited bandwidth of a few layers of MoS_2 [23]. Therefore, the hole electron pair possesses both a greater ability for redox reactions and a greater capacity for UV absorption. The absorption range and utilization of visible light are both lowered by an increase in visible light [24]. Therefore, the optimal photocatalytic performance can only be achieved by preparing the right number of layers of MoS_2 [25]. The MoS_2's primary purpose is to retrieve and store electrons from another semiconductor because of its exceptional electrical conductivity [26]. Catalytic effectiveness is increased by the valence band and its effective transfer to water molecules adsorbed on the catalyst surface [27]. From an alternative perspective, more reactants can be absorbed by the MoS_2 2D film due to its huge specific surface area. It contains several unsaturated bonds and a complicated film edge structure [28]. Furthermore, the heterojunctions of g-C_3N_4 and MoS_2 in this investigation are staggered by the theory [29]. Consequently, light from the valence bands of g-C_3N_4 and MoS_2 can excite electrons when the light source illuminates the semiconductor heterojunction [30]. Currently, the photogenerated electrons in g-C_3N_4 can be readily transported to the MoS_2 conduction band due to their substantial conduction band shift. Photogenerated electrons can be efficiently used because MoS_2 has the chemical potential to enable electrons to combine with protons to form oxygen at hydrogen-producing active sites [31]. In addition, holes can go from MoS_2 to g-C_3N_4 due to the valence band offset of these [32]. This explains why the photo-corrosion issue can be resolved by the aggregation of MoS_2 and g-C_3N_4. As a result, oxidation or reduction reactions react on g-C_3N_4 and MoS_2, respectively, and create a heterojunction bordered by these conjugations of electron holes [33]. Therefore, between metal and non-metal, Te is a metalloid, or semimetal element. The metal's and semiconductor's conductivity [34]. The unique characteristic of semi-metals is their zero or negative bandgaps. As a result, unlike narrow bandgap semiconductors, the electrons in semi-metal materials can move around relatively easily and do not require thermal excitation at the top of the valence band [35]. It will move toward the bottom of the energy guide's lower or equal section. Consequently, a key distinction between semiconductors and metal-like materials is that the semi-metallic conduction band already has a specific electron concentration at absolute zero [36]. At zero degrees Celsius, the substance that will be used in this experiment has a specific electron concentration in the conduction band. Te is thermally stimulated to produce more electrons and holes as the temperature rises. That is, a material's electron concentration is between metal and non-metal, Te is a metalloid, or semimetal element. The conductivity of the metal to semiconductor [37]. The unique characteristic of semi-metals is their zero or negative bandgaps. As a result, unlike narrow bandgap semiconductors, the electrons in semi-metal materials can move around relatively easily and do not require thermal excitation at the top of the valence band. It will move toward the bottom of the energy guide's lower or equal section. A semiconductor is different from a metal-like material based on its electron where a semi-metallic conduction band has a specific electron concentration at absolute zero [38]. At zero temperature, the Te used in this experiment has a specific electron concentration in the conduction band. Te is thermally stimulated to produce more electrons and holes as the temperature rises. When a material has a higher electron concentration and improved conductivity, it can act as a catalyst in a composite photocatalyst and function similarly to

a metal element [39]. Te is a metalloid substance that conducts electricity well.

Herein, we addressed how to increase the hazardous MB dye through the photocatalytic degradation of g-C_3N_4 nanocomposites implanted with tellurium (Te) and MoS_2. When Te and MoS_2 were added, the performance for the degradation of g-C_3N_4 increased. 5 % Te/g-C_3N_4 and 0.2 % MoS_2/g-C_3N_4 were used to test the photocatalytic degradation efficiency of MB (10, 15, and 20 mg/L) solution. Almost 100 % of the MB dye was destroyed in 60 minutes, according to the data, and the photo-catalytic movement to the 5 % Te/g-C_3N_4 composite likewise showed the maximum movement when compared to other produced nanocomposites. As a result, Te can act as a bridge between two semiconductors in the Te/MoS_2/g-C_3N_4 ternary composite, transferring photo-generated carriers, accelerating the pace at which carriers transfer, and suppressing holes and electrons. Composites increase quantum efficiency and extend carrier lifetimes. The purpose of this research is to shed light on the photodegradation process, material design, and risk assessment for the purification of wastewater.

2. Experimental

2.1. Materials

All reagents, e.g., melamine ($C_3H_6N_6$), potassium hydroxide (KOH), ammonium molybdate tetrahydrate {$(NH_4)_6MO_7O_{24}{\cdot}4\ H_2O$}, thiourea ($H_2NCSNH_2$), tellurium (Te), molybdenum sulfide (MoS_2) powder, and methylene blue ($C_{16}H_{18}ClN_3S{\cdot}3\ H_2O$) were supplied from the laboratory with analytical purity. All the solutions were prepared in secondary distilled water (H_2O) with self-controlled purity.

2.2. Preparation of g-C_3N_4

The graphitic carbon nitride (g-C_3N_4) was fabricated using the alkali treatment method. Briefly, 1.0 g of potassium hydroxide powder was taken into a 50-mL beaker, and then 30 mL of distilled water was added. Then 15.0 g of melamine was added to the KOH solution and continuously stirred for 3 hours. When the white, creamy state was obtained, the beaker was placed in an oven at 85 °C and waited until the powder was formed. The powder in the beaker is transferred to the crucible, covered with a lid, and placed in a muffle furnace for heating at 550 °C with a heating rate of 10 °C/min for 4.0 h. The powder was then taken out of the muffle furnace, ground further, and washed with distilled water until the supernatant above the centrifugation was neutral (~3 times). Finally, the precipitate was dried at 85 °C, stored, and labeled as pure g-C_3N_4.

2.3. Preparation of Te/g-C_3N_4 nanocomposites

A 0.4 g tellurium (Te) powder was dispersed in 20 mL distilled water in an ultrasonic cleaner bath for 2–3 h. The mixture was poured into a watch glass and air-dried. The prepared 5 mg Te powder and 0.5 g of the g-C_3N_4 powder were taken with 20 mL distilled water in a 25 mL glass bottle. The mixture was sonicated for half an hour and stirred for one hour placed in a watch glass and dried at 60 ℃ in an oven. The dried powder was uniformly ground and transferred to a porcelain ark, placed in a tube furnace, heated to 200 °C at a heating rate of 5 °C/min, and kept for 2 h. The target mixture was allowed natural cooling and used as a Te/g-C_3N_4 composite.

2.4. Preparation of C-MoS_2/ g-C_3N_4 nanocomposites

A 1.0 mg/mL C-MoS_2 solution was prepared by ultrasonic homogenization. The next 1.0 g of g-C_3N_4 was taken in a small bottle and added dropwise to the C-MoS_2 solution prepared previously. The mixture was stirred for 1.0 h and placed in an ultrasonic bath for 2.0 h. The stirring and sonication are to block the g-C_3N_4 and C-MoS_2 from being automatically peeled into a layer and in full contact, which is conducive to compounding. After 2.0 h, the beaker was placed in an oven and dried at 85 °C. After drying, transfer it to a mortar and grind it to powder, then put it into a tube furnace at 300 °C at a heating rate of 5 °C/min for 2.0 h. After it is naturally cooled, take it out of the calcined materials.

2.5. Characterization of the nanocomposites

X-ray diffraction (XRD), scanning electron microscopy (SEM), and UV–visible diffuse reflectance spectroscopy were used to characterize the structure, morphology, and light absorption range of different nanocomposite samples. The XRD was taken at Bruker AXS, Germany, using a copper Ka target as a radiation source with a step size of 0.01°/2 and a scan range of 5–80°. The SEM topography was scanned by HITACHI's SU8010 ultra-high-resolution field emission scanning electron microscope. The light absorption intensity and range of the solid powder were determined by a Shimadzu UV-2550 ultraviolet-visible spectrometer. The absorbance during the degradation of methylene blue (MB) was detected by a UV-1800PC ultraviolet-visible spectrophotometer.

2.6. Photo-catalytic degradation of methylene blue (MB) dyes analysis

The methylene blue solution of 10 mg/L was taken into a beaker. The original absorbance of the methylene blue solution was measured with a spectrophotometer. The background was calibrated with pure water, and the absorbance of pure water was measured. Water, the absorbance value of the methylene blue solution measured at 665 nm is recorded as the original absorbance A0), then

weighed 0.05 g of the catalyst solution, and added magnets to the beaker. The magnetic force of the beaker was placed in the dark box. Stir on the stirrer until the catalyst reaches the adsorption saturation in the dark environment (after many experiments, the catalyst synthesized in this experiment can reach the adsorption equilibrium within one hour, so unified dark adsorption for 1.0 h). After 1.0 h, a certain amount of liquid was poured out and centrifuged. The supernatant was carefully aspirated into a cuvette and then placed in a UV–visible spectrophotometer sample cell to measure the absorbance. The absorbance at 665 nm was recorded as A1 (A1 is the initial absorbance of photo-catalytic degradation). After measuring A1, the test tube and the solution in the cuvette and the catalyst are recovered, poured back into the beaker, placed on a magnetic stirrer in the dark box, and after the stirring is turned on, the black box door is closed, the light source is turned on, and the timing is started. After irradiating for 30 min, 60 min, 90 min, and 120 min, a certain number of samples were taken, and the absorbance was measured by the same method. The absorbance values at 665 nm were recorded as A2, A3, A4, and A5, respectively. Through the values of A0-A5, we can determine the decolorization rates D, C/C0, and C/C1 of methylene blue at various time points to analyze the adsorption and photocatalytic degradation properties of the catalyst.

3. Results and discussion

3.1. UV–visible diffuse reflectance spectroscopy (UV-Vis) analysis

Fig. 1**(a)** represents the photosensitive regions of g-C_3N_4 and 0.2 % C-MoS_2/g-C_3N_4 and 5 % Te/0.2 % C-MoS_2/ g-C_3N_4 nanocomposites. The photosensitivity of nanocomposites remains similar to that of pristine graphitic nitride, mainly concentrated in the ultraviolet region, with 0.2 % utilization of ultraviolet lights.

The photosensitive regions of g-C_3N_4, S-MoS_2, 0.3 % S-MoS_2/g-C_3N_4, and 5 % Te/0.3 % S-MoS_2/g-C_3N_4 nanocomposites are shown in Fig. 1**(b)**. With 0.3 % of UV light used, the photosensitivity of nanocomposites is still comparable to that of pure graphitic nitride and is mostly focused in the ultraviolet range.

3.2. X-ray diffraction analysis of nanocomposites

It can be seen from Fig. 2**(a)** that both g-C_3N_4 and C-MoS_2 have obvious diffraction peaks, and it can be seen that the g-C_3N4 synthesized in this experiment has higher purity than the commercially available C-MoS_2. The characteristic peak of MoS_2 in 0.2 % C-MoS_2/g-C_3N_4 is not obvious, because the proportion of MoS_2 in the composite is too low or its crystal form is masked by g-C_3N_4. It can be seen from Fig. 2**(b)** that g-C_3N_4 has obvious diffraction peaks, and it can be seen that g-C_3N_4 synthesized in this experiment has higher purity. The synthesized S-MoS_2 did not show obvious characteristic peaks of MoS_2. It can be seen that the MoS_2 synthesized in the experiment is relatively impure. The characteristic peak of MoS_2 in 0.3 % S-MoS_2/g-C_3N_4 is also not obvious, and the XRD pattern of the low proportion of MoS_2/g-C_3N_4 composite synthesized in the experiment of Lei Ge [43] is also not seen. The characteristic peak of MoS_2 can be because the proportion of MoS_2 in the composite is too low or because its crystal form is masked by g-C_3N_4.

3.3. Morphological analysis

The surface morphology of different nanocomposites was analyzed with field emission scanning electron microscopy (FE-SEM). The FE-SEM image of C-MoS_2 and S-MoS_2 (Fig. 3**a-e**) shows that the sheet structure area of C-MoS_2 is larger and thicker, while the sheet structure of S-MoS_2 is smaller and smaller, showing clusters of flowers. Therefore, it is easier to agglomerate than C-MoS_2, and it is not conducive to the compounding of Te in the later stage. Also, we found that 5 % Te/0.2 % C-MoS_2/g-C_3N_4 and 5 % Te/0.3 % S-MoS_2/g-C_3N_4 (Fig. 3**f-h**). 5 % Te/0.2 % C-MoS_2/g-C_3N_4 has a distinct layered structure, while 5 % Te/0.3 % S-MoS_2/g-C_3N_4 experienced more severe agglomeration.

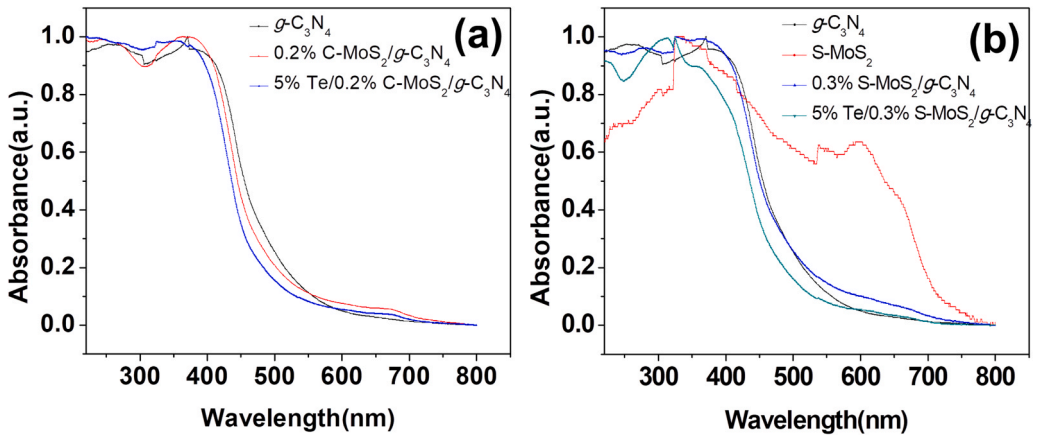

Fig. 1. (a) and (b) UV-Vis diffuses reflectance of the various samples.

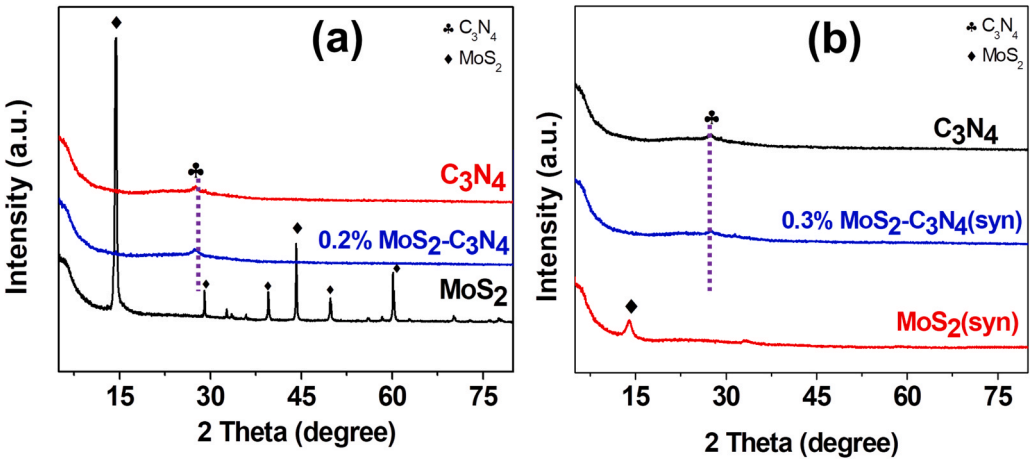

Fig. 2. (a) XRD pattern of g-C_3N_4, C-MoS_2, and 0.2 % C-MoS_2/ g-C_3N_4, (b) XRD pattern of g-C_3N_4, S-MoS_2, and 0.3 % S-MoS_2/ g-C_3N_4.

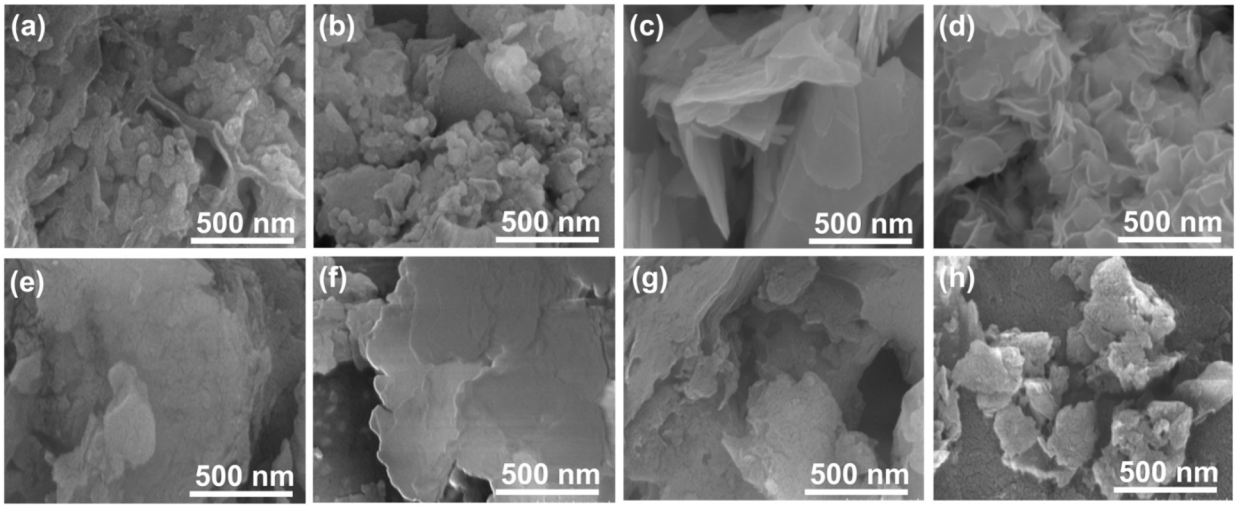

Fig. 3. SEM image: (a) g-C_3N_4 (b) 5 % Te/g-C_3N_4 (c) C-MoS_2 (d) S-MoS_2 (e) 0.2 % C-MoS_2/ g-C_3N_4 (f) 5 % Te/0.2 % C-MoS_2/ g-C_3N_4 (g) 0.3 % S-MoS_2/ g-C_3N_4 (h) 5 % Te/ 0.3 % S-MoS_2/ g-C_3N_4.

It can be seen from Fig. 3**(a)** that g-C_3N_4 appears as a thick layered sheet, and Fig. 3**(b)** shows that a small layer of Te is supported on the surface of the bulk layered g-C_3N_4. In Fig. 3**(c)**, C-MoS_2 exhibits a smooth layered structure, and each layered structure has a large surface area. Still, the thickness is thick, resulting in a small bandgap, which explains why pure MoS_2 does not exhibit photo-catalytic degradation properties. In Fig. 3**(d)**, S-MoS_2 is a thin piece with a large surface area. Figs. 3**(e)** and **(g)** clearly show the two layers of the composite structure together. In Figs. 3**(f)** and **(h)**, respectively, the small particle layer is loaded on the large layer. Explain the successful combination of the three. The sample in Fig. 3**(h)** has a certain degree of agglomeration, so it can explain why its catalytic activity is not as good as 5 % Te/0.2 % C-MoS_2/g-C_3N_4.

3.4. Reactive species play a major role during the degradation process

We confirmed that active species play an important role in the degradation process of novel two-dimensional layered g-C_3N_4 nanocomposites, which can achieve sustainable wastewater treatment through catalytic degradation of methylene blue (MB). Moreover, we also performed experiments on photoactive catalysts to evaluate the impact of photocatalysis on active species production and MB degradation. These experiments and analyses provide a comprehensive understanding of the key active species involved in MB degradation and their mechanisms of action in the process using novel 2D layered g-C_3N_4 nanocomposites.

3.4.1. Degradation efficiency of different proportions of Te/g-C_3N_4 composites

The Te/g-C_3N_4 materials were prepared using ultrasonic calcination under an inert gas atmosphere at a calcination temperature of 200 °C. In a subsequent test for photocatalytic degradation of dye performance, 0.5 g of sample was added to 100 mL of 10 mg/L

methylene blue. After 1.0 h of dark adsorption, the light was started, and the absorbance of the solution was measured once every 0.5 h. In this experiment, a UV-1800PC UV–visible spectrophotometer was used to detect the absorbance of the solution. The absorbance of the solution was positively correlated with the MB concentration of the solution, to make the MB degradation efficiency curve with the abscissa time and the ordinate as C/C_0 as shown in Fig. 4**(a)**, and the kinetic curve with the abscissa is time and the ordinate as $-\ln(C/C_0)$ Fig. 4**(b)**.

Fig. 4**(a)** shows the pure phase g-C_3N_4 and six different proportions of Te/g-C_3N_4 composites after adsorption equilibrium (the solution concentration after adsorption equilibrium is the initial concentration) of light for 2 h to 10 mg/L. The degradation curve of the methylene blue solution shows the difference in the degradation efficiency of different photo-catalysts and the difference in performance between them. Fig. 4**(b)** shows that each photo-catalytic degradation process is consistent with first-order kinetics and that different ratios of composite materials have different K values. We can conclude that in the range of composite ratios we tested, the photo-catalysts of Te were better than pure phase g-C_3N_4, of which 1 %, 3 %, 4 %, and 5 % of the composite products were After 2 h of light, the decolorization rate reached more than 80 %, and the degradation curve of 5 % Te/g-C_3N_4 decreased the most, that is, the highest degradation efficiency and the largest K value. So, we can conclude that 5 % is the optimal ratio of Te/g-C_3N_4 composite photo-catalytic material.

The reason why 5 % of the intermediate portion of the composite ratio is the optimum composite ratio observed is that when Te is too small, Te cannot be sufficiently compounded with g-C_3N_4 to function as a co-catalyst. When Te is high, agglomeration tends to occur, and the surface of g-C_3N_4 recombines the absorption of light by g-C_3N_4, thereby affecting the catalytic efficiency.

3.4.2. Degradation efficiency of different ratios of C-MoS_2/ g-C_3N_4 binary composites

The C-MoS_2/g-C_3N_4 composite was prepared by ultrasonic calcination under an inert gas atmosphere at a calcination temperature of 300 °C. Fig. 5**(a)** shows six different ratios of the pure phase of g-C_3N_4 and the combination of C-MoS_2/g-C_3N_4 at 2 h to 10 mg of light synthesis (initial concentration of solution concentration after adsorption equilibrium). The degradation curve of the methylene blue solution also shows the degradation efficiency of different photocatalysts and the difference in performance between them. Fig. 5**(b)** shows that each photo-catalytic degradation process is consistent with first-order kinetics and that different ratios of composite materials have different K values. We can conclude that the photo-catalysts of MoS_2 are better than the pure phase g-C_3N_4 in the range of composite ratios we tested, and the degradation curve of 0.2 % C-MoS_2/g-C_3N_4 is the largest. The K value is the largest, that is, the highest degradation efficiency, so we can conclude that 0.2 % is the best proportion of C-MoS_2/g-C_3N_4 composite photo-catalytic material.

The combination of a small amount of layered MoS_2 and g-C_3N_4 can completely hinder the agglomeration of g-C_3N_4, and the presence of g-C_3N_4 can also prevent the agglomeration of MoS_2 and form a heterostructure between them, increasing the range of photo response and increasing quantum yield. However, when the number of MoS_2 molecules is large, MoS_2 itself is prone to agglomeration. Secondly, when too much MoS_2 is compounded on the surface of g-C_3N_4, the distance of electron transport will be lengthened, which is not conducive to the efficient transmission of electrons and thus affects the catalytic efficiency and will cover Part of the surface of g-C_3N_4 catalyzes the active site, thereby affecting its catalytic efficiency.

3.4.3. Degradation efficiency and repeatability

The preparation method was the same as Te/g-C_3N_4, and the raw material g-C_3N_4 was replaced with 0.2 % C-MoS_2/g-C_3N_4. Fig. 6**(a)** shows the pure phase g-C_3N_4, the optimum ratio of 0.2 % C-MoS_2/g-C_3N_4 composite, and 5 % Te/0.2 % C-MoS_2/g-C_3N_4 composite after adsorption equilibrium (after adsorption equilibrium) (degradation curve of 10 mg/L methylene blue solution within 2.0 h of light at a solution concentration of the initial concentration). We can conclude that the photo-catalytic activity of the 5 % Te/0.2 % C-MoS_2/g-C_3N_4 ternary composite prepared based on the 0.2 % C-MoS_2/g-C_3N_4 composite is less than that of the 0.2 % C-MoS_2/g-C_3N_4 binary composite.

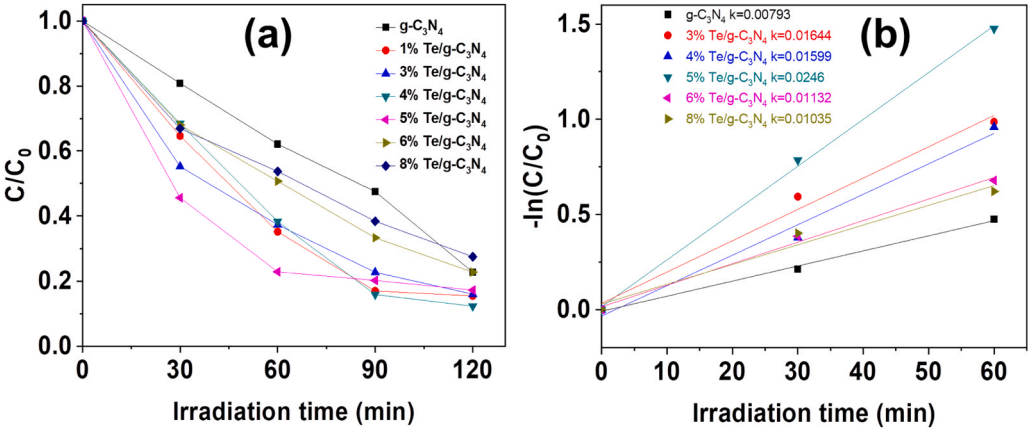

Fig. 4. (a) Photo-catalytic degradation of MB curve, and (b) -ln (Ct /C_0) of Te/ g-C_3N_4 composites with light time curve.

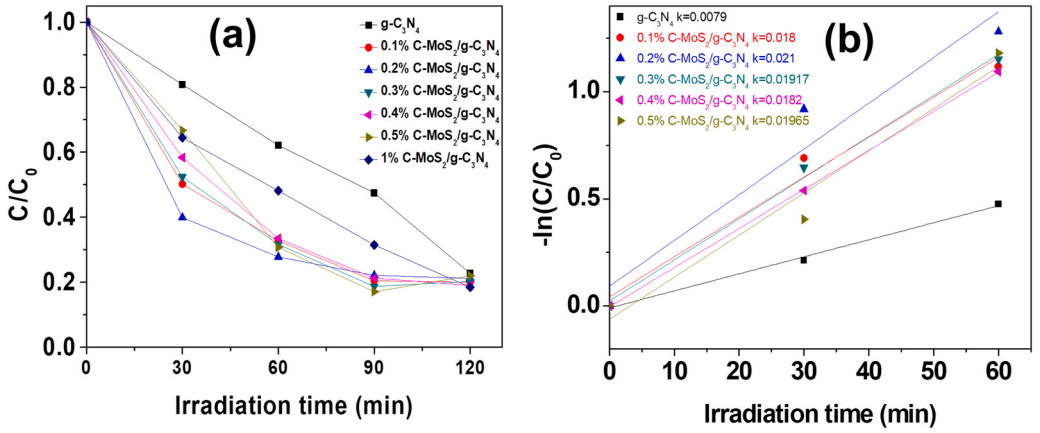

Fig. 5. (a) C-MoS_2/ g-C_3N_4 photo-catalytic degradation of MB curve and (b) -ln (Ct /C_0) with light time curve.

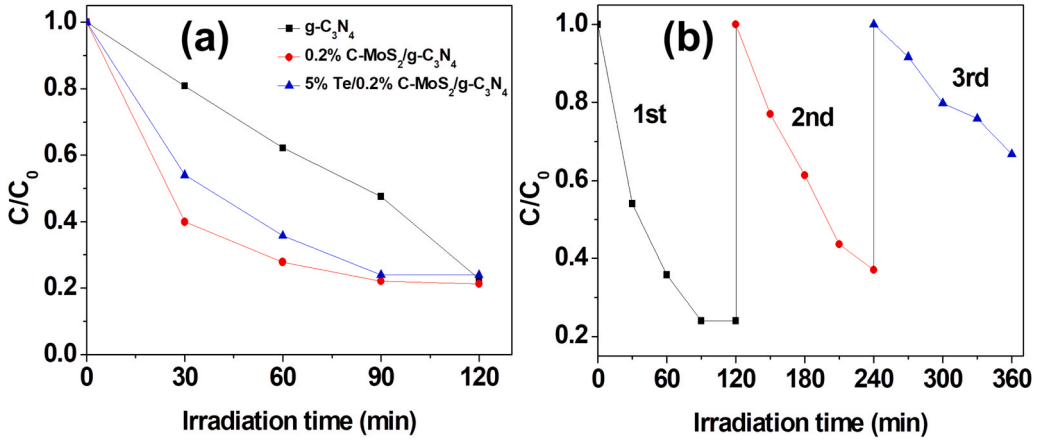

Fig. 6. (a) Photo-catalytic degradation of MB curve by 5 % Te/ 0.2 % C-MoS_2/ g-C_3N_4 ternary composite, (b) Repeatability experiment of photo-catalytic degradation of MB in 5 % Te/ 0.2 % C-MoS_2/ g-C_3N_4 composite.

This can be because Te, as an electron transport bridge, does not control its composite ratio, which causes Te to become a recombination canter of photo-generated electrons emitted by g-C_3N_4 and photo-generated holes released by MoS_2, resulting in a quantum efficiency reduction. It can be seen from Fig. 6**(b)** that the catalytic efficiency of the composites continued to decrease in the reproducibility experiments of the 1–3 groups. In the second set of repeated experiments, the catalytic efficiency decreased less than

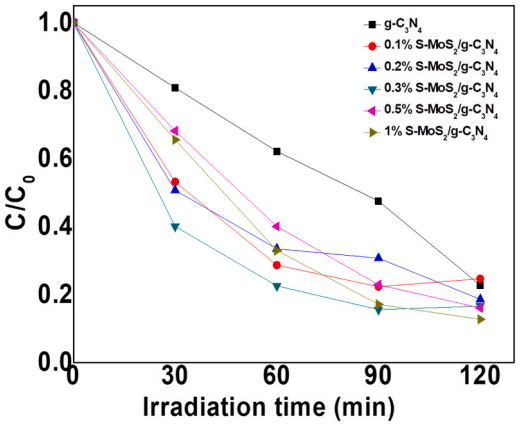

Fig. 7. The photocatalytic degradation efficiency of different proportions of S-MoS_2/ g-C_3N_4 binary composites.

that of the first group, but not in the third group of experiments. A large drop occurred, and the decolorization rate could not reach 50 % after 2 h of illumination. It can be seen that the 5 % Te/0.2 % C-MoS_2/g-C_3N_4 composite material has poor cycle ability.

3.4.4. Degradation efficiency of different proportions of S-MoS_2/ g-C_3N_4 binary composites

The preparation method was the same as that of C-MoS_2/g-C_3N_4, and the raw material C-MoS_2 was replaced by S-MoS_2. Six different ratios (2 h to 10 mg/L) of light-synthesis (concentration of solution after synthesis equilibrium, initial concentration) light after pure phase g-C_3N_4 and brief equivalence of S-MoS_2/g-C_3N_4 binary composites are shown in Fig. 7. The degradation curve of methylene blue solution shows the difference in degradation efficiency of different photocatalysts and the difference in performance between them.

3.4.5. Degradation efficiency and repeatability of 5 % Te/ 0.3 % S-MoS_2/ g-C_3N_4

The preparation method was the same as Te/g-C_3N_4, and the raw material g-C_3N_4 was replaced with 0.3 % S-MoS_2/g-C_3N_4. Fig. 8 **(a)** shows the photocatalytic degradation of the MB curve of the 5 % Te/0.3 % S-MoS_2/g-C_3N_4 composite after adsorption equilibrium of the 10 mg/L degradation curve of the methylene blue solution within 2 h of frequent lighting of the initial concentration solution. We can conclude that the photo-catalytic activity of the 5 % Te/0.3 % C-MoS_2/g-C_3N_4 ternary composite prepared based on the 0.3 % C-MoS_2/g-C_3N_4 composite is less than that of the 0.3 % C-MoS_2/g-C_3N_4 binary composite. This can be because Te, the electron transport, as a bridge, does not control its composite ratio, causing the photo-generator emitted by g-C_3N_4 to become a rehabilitation canter of electrons, and the photo-generated pores released by MoS_2 result in quantum decreased efficiency.

Also, it can be seen from Fig. 8**(b)** that the catalytic efficiency of the composite material continues to decrease in the repeatability experiments of 1–2 groups. In the second set of repeated experiments, the catalytic efficiency of the catalyst is significantly greater than in the first set of experiments. The decline in decolorization rate after 2 h of illumination still cannot reach 50 %, showing that the 5 % Te/0.3 % S-MoS_2/g-C_3N_4 composite material has poor cycle ability.

3.4.6. Comparison between commercial MoS_2 composites and synthetic MoS_2 composites

The performance compares the optimal ratio of C-MoS_2/g-C_3N_4 and S-MoS_2/g-C_3N_4 binary composites. It can be seen from Fig. 9**(a)** that the optimal ratio of the synthetic MoS_2 binary composite (i.e., 0.3 % S-MoS_2/g-C_3N_4) is slightly more photo-catalytic than the commercial MoS_2 binary composite (i.e., 0.2 % C-MoS_2/g-C_3N_4). Probably, the synthesized MoS_2 has a thin sheet structure when a heterojunction is formed with the layered g-C_3N_4. The transfer time of the photo-generated carriers is shorter, so the catalytic efficiency is higher.

Also, the performance has been compared between Te/C-MoS_2/g-C_3N_4 and Te/S-MoS_2/g-C_3N_4 ternary composites. It can be seen from Fig. 9**(b)** that the photo-catalytic degradation performance and recyclability of the commercial MoS_2 ternary composite (i.e., 5 % Te/0.2 % C-MoS_2/g-C_3N_4) are stronger than those of the synthetic MoS_2 ternary composite (i.e., 5 % Te/0.3 % S-MoS_2/g-C_3N_4).

3.4.7. Photo-catalytic degradation efficiency of different concentrations of MB

Fig. 10 shows the illumination of a 5 % Te/0.2 % C-MoS_2/g-C_3N_4 composite product after adsorption at 10 mg/L, 15 mg/L, and 20 mg/L MB solution for 30 min and 60 min, with degradation efficiency at 90 min and 120 min. We can observe that the 5 % Te/0.2 % C-MoS_2/g-C_3N_4 composite product has the most efficient degradation efficiency in 10 mg/L MB solution and the lowest degradation efficiency in 20 mg/L MB solution. Also, we can optimize that within the range of MB concentrations tested (i.e., 10–20 mg/L), the degradation efficiency decreased with increasing MB concentration. When the dye concentration is increased, the degradation effect of the photocatalyst can be due to the increase in the MB concentration, which causes the chromaticity of the solution to increase, resulting in a decrease in the transmittance of the solution, which hinders 5 % Te/0.2 % C-MoS_2/g-C_3N_4, and the

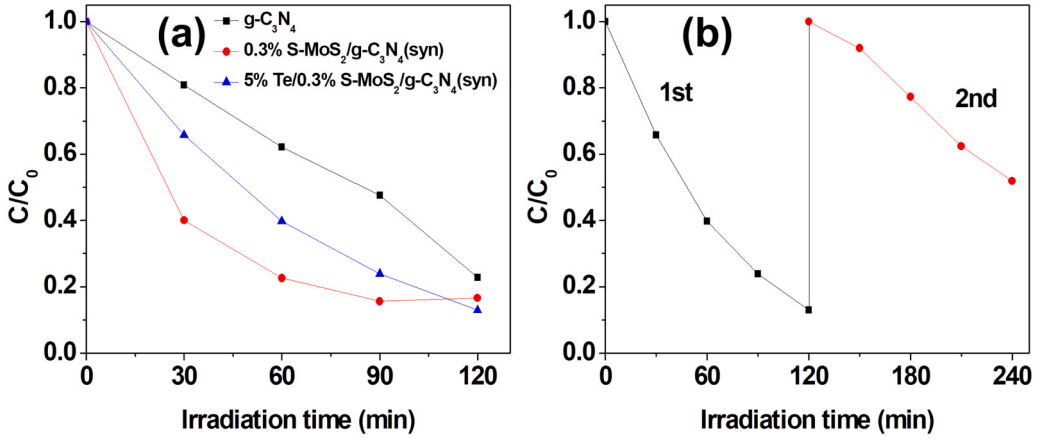

Fig. 8. (a) Photo-catalytic degradation of MB curve of 5 % Te/ 0.3 % S-MoS_2/ g-C_3N_4 composite, (b) Reproducibility of photo-catalytic degradation of MB in 5 % Te/ 0.3 % S-MoS_2/ g-C_3N_4 composite.

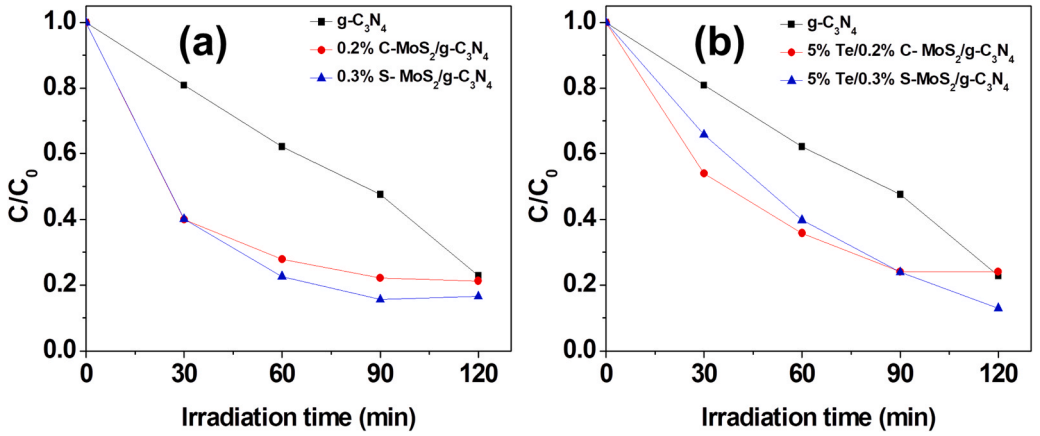

Fig. 9. (a) Photo-catalytic degradation of MB by 0.2 % C-MoS_2/ g-C_3N_4 and 0.3 % S-MoS_2/ g-C_3N_4; (b) Photo-catalytic degradation of MB by 5 % Te/ 0.2 % C-MoS_2/ g-C_3N_4 and 5 % Te/ 0.3 % S-MoS_2/ g-C_3N_4.

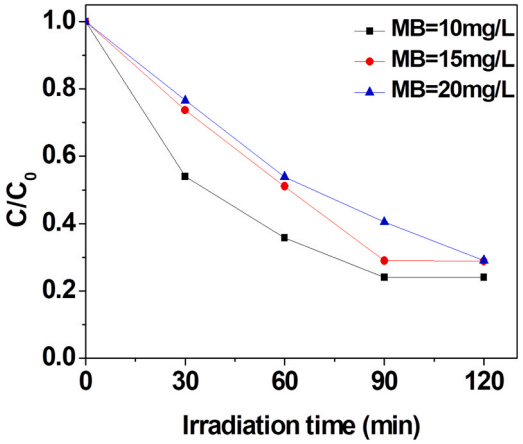

Fig. 10. The photo-catalytic experiments of 5 % Te/ 0.2 % C-MoS_2/ g-C_3N_4 composite product in different concentrations of MB solution.

contact of light affects its light absorption rate [44].

3.4.8. Te/ g-C_3N_4 composite photo-catalyst mechanism diagram

As shown in Fig. 11, when Te is supported on the surface of g-C_3N_4, g-C_3N_4 is photo-excited to generate photo-generated electrons and holes based on the internal surface, failing to function. There is also a part of photo-generated electrons that flow to Te due to its excellent conductivity; that is, Te forms an electron barrier. Therefore, photo-generated electrons and holes are respectively localized on Te and g-C_3N_4, and the reconsolidation rate of the photo-generated transporter is lowered. Improve the efficiency of degrading pollutants.

3.4.9. MoS_2/g-C_3N_4 semiconductor heterojunction photo-catalyst mechanism diagram

As shown in Fig. 12, the lamellar g-C_3N_4 is combined with MoS_2. The sensitization of the narrow-band semiconductor MoS_2 can extend the photo-response range of the photocatalyst, and the contact interface between g-C_3N_4 and MoS_2 forms a built-in electric field. It can promote the separation of photo-generated electrons and holes, inhibit their recombination, and improve quantum yield. The good conductivity of MoS_2 facilitates its reception and stockpile taken away to g-C_3N_4, improves lifetime photo-generated electrons, and efficiently transfers to the dye solution adsorbed on its surface, thereby improving degradation efficiency.

3.4.10. Mechanism of Te/ MoS_2/ g-C_3N_4 ternary composite semiconductor photo-catalyst

The Te, MoS_2, and g-C_3N_4 are connected to each other. In the ternary composite, two binary compounds, MoS_2/g-C_3N_4, and Te/g-C_3N_4, are also mentioned in Fig. 13. The mechanism of action affects the photo-catalytic efficiency, and on this basis, the synthesis of ternary complexes constructs a Z-type heterostructure [40-42, 45-48], which optimizes the electron transport at the heterojunction interface. Te builds a bridge with good conductivity between g-C_3N_4 and MoS_2, which acts as an electron transfer, accelerates electron transfer, increases quantum yield, and increases photo-catalytic degradation efficiency.

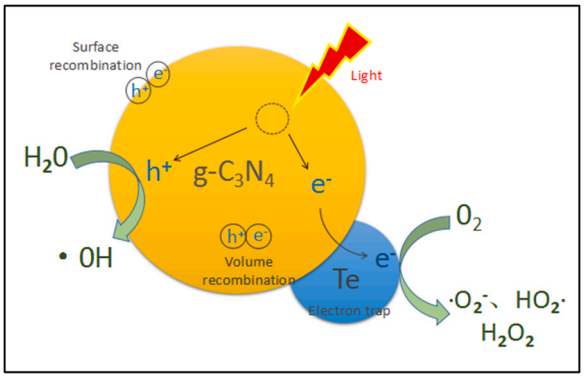

Fig. 11. Mechanism diagram of Te/g-C_3N_4 binary composite.

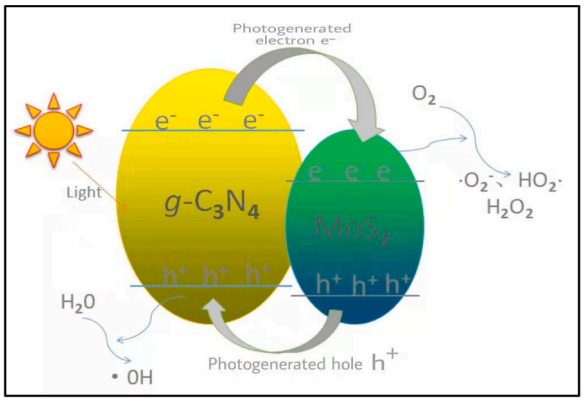

Fig. 12. MoS_2/g-C_3N_4 semiconductor heterojunction photo-catalyst mechanism diagram.

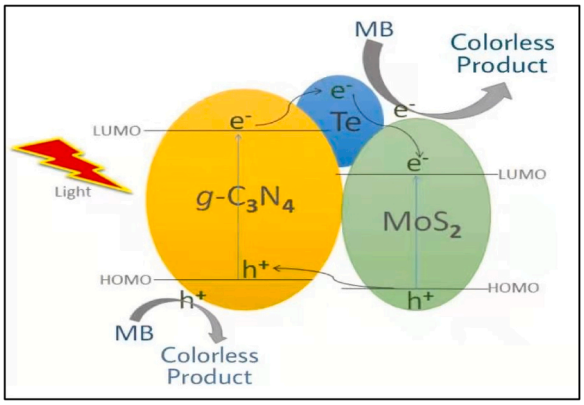

Fig. 13. Mechanism diagram of Te/ MoS_2/ g-C_3N_4 ternary composite semiconductor photo-catalyst.

4. Conclusions

The photocatalytic degradation of MoS_2 and tellurium (Te) embedded g-C_3N_4 nanocomposites for enhanced toxic MB dye was discussed. The performance of the degradation of g-C_3N_4 was promoted according to the incorporation of Te and MoS_2. The photo-catalytic degradation efficiency of MB (10, 15, and 20 mg/L) solution was investigated with 5 % Te/g-C_3N_4 and 0.2 % MoS_2/g-C_3N_4. The data disclosed that the photo-catalytic movement of the 5 % Te/g-C_3N_4 composite also exhibited the highest compared with other prepared nanocomposites, and almost 100 % of the MB dye was degraded within 60 min. The degradation efficiency of g-C_3N_4 nanocomposites decreased with an increase in MB concentration, and the degradation rate of MB was ~1.5 mg/L. The measured properties and pure phase of 2D-layered nano-g-C_3N_4 semiconductor materials were obtained. It also compares the photo-catalytic

activities of different composite ratios, including the best MoS_2 composite ratio. Two series of g-C_3N_4/MoS_2 were combined with commercial MoS_2 and synthetic MoS_2, respectively. The optimal proportion of Te/g-C_3N_4 and the maximum proportion of g-C_3N_4/MoS_2 with certain levels of Te were carried out at the photo-catalytic degradation issues. Therefore, the Te-embedded g-C_3N_4 nanocomposites would be an effective material to degrade toxic MB dyes from wastewater.

CRediT authorship contribution statement

Most Munera Khatun: Writing – original draft, Formal analysis, Data curation, Conceptualization. **Mohammad Raza Miah:** Writing – original draft, Data curation, Conceptualization. **Chunjie Yan:** Resources, Methodology, Investigation, Conceptualization, Project administration, Supervision, Funding acquisition. **Most Foijunnesa**: Writing – original draft, Formal analysis, Data curation, Conceptualization. **M.Mahbubul Bashar:** Investigation, Formal analysis, Data curation, Writing – review & editing. **Shahjalal Khandaker:** Resources, Methodology, Investigation, Conceptualization. **Takahiro Kuba:** Visualization, Validation, Formal analysis, Investigation. **Khalid A. Alzahrani:** Visualization, Validation, Formal analysis, Investigation. **M.A. Shenashen:** Visualization, Validation, Formal analysis, Investigation. **Mohammed M. Rahman:** Visualization, Validation, Formal analysis, Investigation. **Abdullah M. Asiri:** Visualization, Validation, Formal analysis, Investigation. **Aminul Islam:** Visualization, Validation, Methodology, Formal analysis, Data curation. **Munjur Hasan:** Validation, Software, Project administration, Investigation. **Rabiul Awual:** Writing – review & editing, Supervision, Funding acquisition.

Declaration of Competing Interest

The authors declare that they have no known competing financial interests or personal relationships that could have appeared to influence the work reported in this paper.

Data availability

The data that has been used is confidential.

Acknowledgments

This work is supported by the Hubei Provincial Natural Science Foundation of China (No. 2020CFA037, 2020CFB356) and the Fundamental Research Funds for the Central Universities, China University of Geosciences (Wuhan) (No. 162301202617), for which the authors wish to express their great appreciation.

References

[1] H. Jiang, Y. Li, D. Wang, X. Hong, B. Liang, Recent advances in heteroatom doped graphitic carbon nitride (g-C_3N_4) and g-C_3N_4/metal oxide composite photocatalysts, Curr. Org. Chem. 24 (6) (2020) 673–693.
[2] K.T. Kubra, M.S. Salman, M.N. Hasan, Enhanced toxic dye removal from wastewater using biodegradable polymeric natural adsorbent, J. Mol. Liq. 328 (2021) 115468.
[3] W. Zhang, W. Gao, X. Zhang, Z. Li, G. Lu, Surface spintronics enhanced photo-catalytic hydrogen evolution: mechanisms, strategies, challenges and future, Appl. Surf. Sci. 434 (2018) 643–668.
[4] M.S. Salman, H. Znad, M.N. Hasan, M.M. Hasan, Optimization of innovative composite sensor for Pb(II) detection and capturing from water samples, Microchem. J. 160 (2021) 105765.
[5] M.N. Hasan, M.S. Salman, A. Islam, H. Znad, M.M. Hasan, Sustainable composite sensor material for optical cadmium(II) monitoring and capturing from wastewater, Microchem. J. 161 (2021) 105800.
[6] Y. Ma, X. Yang, G. Gao, Z. Yan, H. Su, B. Zhang, Y. Zhang, Photocatalytic partial oxidation of methanol to methyl formate under visible light irradiation on Bi-doped TiO_2 via tuning band structure and surface hydroxyls, RSC Adv. 10 (52) (2020) 31442–31452.
[7] W. Kong, X. Zhang, B. Chang, Y. Zhou, S. Zhang, G. He, J. Li, Fabrication of B doped g-C_3N_4/TiO_2 heterojunction for efficient photoelectrochemical water oxidation, Electrochim. Acta 282 (2018) 767–774.
[8] J.Y. Niu, L. Wang, J.C. Xu, H.X. Jin, B. Hong, D.F. Jin, X.L. Peng, H.L. Ge, X.Q. Wang, Mesoporous Co_3O_4 nanowires decorated with g-C_3N_4 nanosheets for high performance toluene gas sensors based on p-n heterojunction, Mater. Chem. Phys. 293 (2023) 126980.
[9] A. Shahat, K.T. Kubra, M.S. Salman, M.N. Hasan, M.M. Hasan, Novel solid-state sensor material for efficient cadmium(II) detection and capturing from wastewater, Microchem. J. 164 (2021) 105967.
[10] Y. Zeng, X. Zhan, B. Hong, Y. Xia, Y. Ding, T. Cai, K. Yin, X. Wang, L. Yang, S. Luo, Surface atom rearrangement on carbon nitride for enhanced photocatalysis degradation of antibiotics under visible light, Chem. Eng. J. 452 (2023) 139434.
[11] M.S. Salman, M.N. Hasan, K.T. Kubra, M.M. Hasan, Optical detection and recovery of Yb(III) from waste sample using novel sensor ensemble nanomaterials, Microchem. J. 162 (2021) 105868.
[12] T. Xiong, W. Cen, Y. Zhang, F. Dong, Bridging the g-C_3N_4 interlayers for enhanced photocatalysis, ACS Catal. 6 (4) (2016) 2462–2472.
[13] X. Yu, S.F. Ng, L.K. Putri, L.L. Tan, A.R. Mohamed, W.J. Ong, Point-defect engineering: leveraging imperfections in graphitic carbon nitride (g-C_3N_4) photocatalysts toward artificial photosynthesis, Small 17 (48) (2021) 2006851.
[14] X. Liu, Y. Yang, H. Li, Z. Yang, Y. Fang, Visible light degradation of tetracycline using oxygen-rich titanium dioxide nanosheets decorated by carbon quantum dots, J. Chem. Eng. 408 (2021) 127259.
[15] K.T. Kubra, M.S. Salman, H. Znad, M.N. Hasan, Efficient encapsulation of toxic dye from wastewater using biodegradable polymeric adsorbent, J. Mol. Liq. 329 (2021) 115541.
[16] (a) M. Liu, B.F. White, P. Praveen, W. Li, F. Lin, H. Wu, R. Li, C. Delaine, B.E. Forbes, J.D. Wade, M.A. Hossain, Engineering of a biologically active insulin dimer, J. Med. Chem. 64 (2021) 17448–17454;
(b) R.V. Pustovit, X. Zhang, J.J.M. Liew, P. Praveen, M. Liu, A. Koo, L. Oparija-Rogenmozere, Q. Ou, M. Kocan, S. Nie, R.A.D. Bathgate, J.B. Furness, M. A. Hossain, A novel antagonist peptide reveals a physiological role of insulin-like peptide 5 in control of colorectal function, ACS Pharmacol. Transl. Sci. 4 (2021) 1665–1674;

(c) J.A. Karas, J.D. Wade, M.A. Hossain, The chemical synthesis of Insulin: an enduring challenge, Chem. Rev. 121 (2021) 4531–4560;
(d) M.A. Hossain, R. Okamoto, J.A. Karas, P. Praveen, M. Liu, B.E. Forbes, J.D. Wade, Y. Kajihara, Total chemical synthesis of a nonfibrillating human glycoinsulin, J. Am. Chem. Soc. 142 (2020) (2020) 1164–1169;
(e) J.A. Karas, N.A. Patil, J. Tailhades, M.A. Sani, D.B. Scanlon, B.E. Forbes, J. Gardiner, F. Separovic, J.D. Wade, M.A. Hossain, Total chemical synthesis of an intra-A-chain cystathionine human insulin analogue that has enhanced thermal stability, Angew. Chem. Int. Ed. Engl. 55 (2016) 14743–14747.
[17] G.H. Al-Hazmi, M.S. Refat, K.F. Alshammari, K.T. Kubra, A. Shahat, Efficient toxic doxorubicin hydrochloride removal from aqueous solutions using facial alumina nanorods, J. Mol. Struct. 1272 (2023) 134187.
[18] A. Shahat, K.T. Kubra, A. El-marghany, Equilibrium, thermodynamic and kinetic modeling of triclosan adsorption on mesoporous carbon nanosphere: optimization using Box-Behnken design, J. Mol. Liq. 383 (2023) 122166.
[19] (a) K. Aamir, H.U. Khan, G. Sethi, M.A. Hossain, A. Arya, Wnt signaling mediates TLR pathway and promote unrestrained adipogenesis and metaflammation: therapeutic targets for obesity and type 2 diabetes, Pharmacol. Res. 152 (2020) 104602;
(b) W. Li, N.M. O'Brien-Simpson, J. Tailhades, N. Pantarat, R.M. Dawson, L. Otvos, E.C. Reynolds, F. Separovic, M.A. Hossain, J.D. Wade, Multimerization of a proline-rich antimicrobial peptide, Chex-Arg20, alters its mechanism of interaction with the Escherichia coli membrane, Chem. Biol. 22 (2015) 1250–1258;
(c) R.A.D. Bathgate, M.H.Y. Oh, W.J.J. Ling, Q. Kaas, M.A. Hossain, P.R. Gooley, K.J. Rosengren, Elucidation of relaxin-3 binding interactions in the extracellular loops of RXFP3, Front. Endocrinol. 4 (2013) 13;
(d) L.M. Haugaard-Jonsson, M.A. Hossain, N.L. Daly, R.A.D. Bathgate, J.D. Wade, D.J. Craik, K.J. Rosengren, Structure of the R3/I5 chimeric relaxin peptide, a selective GPCR135 and GPCR142 agonist, J. Biol. Chem. 283 (2008) 23811–23818;
(e) M.A. Hossain, B.C.S. Man, C. Zhao, Q. Xu, X.J. Du, J.D. Wade, C.S. Samuel, H3 relaxin demonstrates antifibrotic properties via the RXFP1 receptor, Biochemistry 50 (2011) 1368–1375.
[20] (a) N.A. Patil, J. Tailhades, J.A. Karas, F. Separovic, J.D. Wade, M.A. Hossain, A one-pot chemically cleavable bis-linker tether strategy for the synthesis of heterodimeric peptides, Angew. Chem. Int. Ed. Engl. 55 (2016) 14552–14556;
(b) M.A. Hossain, M. Kocan, S.T. Yao, S.G. Royce, V.B. Nair, C. Siwek, N.A. Patil, I.P. Harrison, K.J. Rosengren, S. Selemidis, R.J. Summers, J.D. Wade, R.A. D. Bathgate, C.S. Samuel, A single chain derivative of the relaxin hormone is a functionally selective agonist of the G protein-coupled receptor, RXFP1, Chem. Sci. 7 (2016) 3805–3819;
(c) N.A. Patil, R.A. Hughes, K.J. Rosengren, M. Kocan, S.Y. Ang, J. Tailhades, F. Separovic, R.J. Summers, J. Grosse, J.D. Wade, R.A.D. Bathgate, M.A. Hossain, Engineering of a novel simplified human insulin-like peptide 5 agonist, J. Med. Chem. 59 (2016) 2118–2125;
(d) J.A. Karas, D.B. Scanlon, B.E. Forbes, I. Vetter, R.J. Lewis, J. Gardiner, F. Separovic, J.D. Wade, M.A. Hossain, 2-nitroveratryl as a photocleavable thiol-protecting group for directed disulfide bond formation in the chemical synthesis of insulin, Chem. Eur. J. 20 (2014) 9549–9552;
(e) A. Belgi, R.A.D. Bathgate, M. Kocan, N. Patil, S. Zhang, G.W. Tregear, J.D. Wade, M.A. Hossain, Minimum active structure of insulin-like peptide 5, J. Med. Chem. 56 (2013) 9509–9516.
[21] K. Hu, X. Hu, Y. Xu, X. Pan, The effect of morphology and size on the photocatalytic properties of MoS_2, React. Kinet. Mech. Catal. 100 (1) (2010) 153–163.
[22] Z. Sun, A. Martinez, F. Wang, Optical modulators with 2D layered materials, Nat. Photon. 10 (4) (2016) 227–238.
[23] Q. Jiang, S. Wang, X. Li, Z. Han, C. Zhao, T. Di, Z. Cheng, Controllable growth of MoS_2 nanosheets on TiO_2 burst nanotubes and their photocatalytic activity, RSC Adv. 10 (67) (2020) 40904–40915.
[24] S. Li, M. Zhang, Z. Qu, X. Cui, Z. Liu, C. Piao, Y. Song, Fabrication of highly active Z-scheme Ag/g-C_3N_4-Ag-Ag_3PO_4 (1 1 0) photocatalyst for visible light photocatalytic degradation of levofloxacin with simultaneous hydrogen production, J. Chem. Eng. 382 (2020) 122394.
[25] X. Zhang, R. Zhang, S. Niu, J. Zheng, C. Guo, Enhanced photo-catalytic performance by effective electron-hole separation for MoS_2 inlaying in g-C_3N_4 hetero-junction, Appl. Surf. Sci. 475 (2019) 355–362.
[26] O.V. Yazyev, A. Kis, MoS_2 and semiconductors in the flatland, Materials 18 (1) (2015) 20–30.
[27] X. Du, J. Huang, J. Zhang, Y. Yan, C. Wu, Y. Hu, J. Xiong, Modulating electronic structures of inorganic nanomaterials for efficient electrocatalytic water splitting, Angew. Chem. 58 (14) (2019) 4484–4502.
[28] S. Li, S. Wang, M.M. Salamone, A.W. Robertson, S. Nayak, H. Kim, J.H. Warner, Edge-enriched 2D MoS_2 thin films grown by chemical vapor deposition for enhanced catalytic performance, ACS Catal. 7 (1) (2017) 877–886.
[29] (a) L.J. Chan, M.A. Hossain, C.S. Samuel, F. Separovic, J. D. Wade, The relaxin peptide family-structure, function and clinical applications, Protein Pept. Lett. 18 (2011) 220–229;
(b) A. Sethi, S. Bruell, N. Patil, M.A. Hossain, D.J. Scott, E.J. Petrie, R.A.D. Bathgate, P.R. Gooley, The complex binding mode of the peptide hormone H2 relaxin to its receptor RXFP1, Nat. Commun. 7 (2016) 11344;
(c) M.A. Hossain, J.D. Wade, Synthetic relaxins, Curr. Opin. Chem. Biol. 22 (2014) 47–55;
(d) S.M. Chowdhury, S.A. Talukder, A.M. Khan, N. Afrin, M.A. Ali, R. Islam, R. Parves, A.A. Mamun, M.A. Sufian, M.N. Hossain, M.A. Hossain, M.A. Halim, Antiviral peptides as promising therapeutics against SARS-CoV-2, J. Phys. Chem. B 123 (2020) 9785–9792;
(e) C. Zhang, B.E. Chua, A. Yang, F. Shabanpoor, M.A. Hossain, J.D. Wade, K.J. Rosengren, C.M. Smith, A.L. Gundlach, Central relaxin-3 receptor (RXFP3) activation reduces elevated, but not basal, anxiety-like behaviour in C57BL/6J mice, Behav. Brain Res. 292 (2015) 125–132.
[30] (a) L.M. Haugaard-Jönsson, M.A. Hossain, N.L. Daly, D.J. Craik, J.D. Wade, K.J. Rosengren, Structure of human insulin-like peptide 5 and characterization of conserved hydrogen bonds and electrostatic interactions within the relaxin framework, Biochem. J. 419 (2009) 619–627;
(b) A. Blasiak, T. Blasiak, M.H. Lewandowski, M.A. Hossain, J.D. Wade, A.L. Gundlach, Relaxin-3 innervation of the intergeniculate leaflet of the rat thalamus – neuronal tract-tracing and in vitro electrophysiological studies, Eur. J. Neurosci. 37 (2013) 1284–1294;
(c) S. Zhang, F. Lin, M.A. Hossain, F. Shabanpoor, G.W. Tregear, J.D. Wade, Simultaneous post-cysteine (S-Acm) group removal quenching of iodine and isolation of peptide by one step ether precipitation, Int. J. Pept. Res. Ther. 14 (2008) 301–305;
(d) J. Tailhades, N.A. Patil, M.A. Hossain, J.D. Wade, Intramolecular acyl transfer in peptide and protein ligation and synthesis, J. Pept. Sci. 21 (2015) 139–147;
(e) M.A. Hossain, C.S. Samuel, C. Binder, T.D. Hewitson, G.W. Tregear, J.D. Wade, R.A.D. Bathgate, The chemically synthesized human relaxin-2 analog, B-R13/17K H2, is an RXFP1 antagonist, Amino Acids 39 (2010) 409–416.
[31] (a) M.A. Hossain, F. Lin, S. Zhang, T. Ferraro, R.A. Bathgate, G.W. Tregear, J.D. Wade, Regioselective disulfide solid phase synthesis, chemical characterization and in vitro receptor binding activity of equine relaxin, Int. J. Pept. Res. Ther. 12 (2006) 211–215;
(b) K. Hojo, M.A. Hossain, J. Tailhades, F. Shabanpoor, L.L.L. Wong, E.E.K. Ong-Pålsson, H.E. Kastman, S. Ma, A.L. Gundlach, K.J. Rosengren, J.D. Wade, R.A. D. Bathgate, Development of a single-chain peptide agonist of the relaxin-3 receptor using hydrocarbon stapling, J. Med. Chem. 59 (2016) 7445–7456;
(c) R. Mirzaei, A. Attar, S. Papizadeh, A.S. Jeda, S.R. Hosseini-Fard, E. Jamasbi, S. Kazemi, S. Amerkani, G.R. Talei, P. Moradi, S. Jalalifar, R. Yousefimashouf, M.A. Hossain, H. Keyvani, S. Karampoor, The emerging role of probiotics as a mitigation strategy against coronavirus disease 2019 (COVID-19), Arch. Virol. 166 (2021) 1819–1840;
(d) C.S. Samuel, F. Lin, M.A. Hossain, C. Zhao, T. Ferraro, R.A.D. Bathgate, G.W. Tregear, J.D. Wade, Improved chemical synthesis and demonstration of the relaxin receptor binding affinity and biological activity of mouse relaxin, Biochemistry 46 (2007) 5374–5381;
(e) M.A. Hossain, H. Mihara, A. Ueno, Fluorescence resonance energy transfer in a novel cyclodextrin–peptide conjugate for detecting steroid molecules, Bioorg. Med. Chem. Lett. 15 (2003) 4305–4308.
[32] (a) F. Shabanpoor, R.A.D. Bathgate, A. Belgi, L.J. Chan, V.B. Nair, J.D. Wade, M.A. Hossain, Site-specific conjugation of a lanthanide chelator and its effects on the chemical synthesis and receptor binding affinity of human relaxin-2 hormone, Biochem. Biophys. Res. Commun. 420 (2012) 253–256;
(b) N.A. Diepenhorst, E.J. Petrie, C.Z. Chen, A. Wang, M.A. Hossain, R.A.D. Bathgate, P.R. Gooley, Investigation of interactions at the extracellular loops of the relaxin family peptide receptor 1 (RXFP1), J. Biol. Chem. 289 (2014) 34938–34952;
(c) J.D. Wade, F. Lin, M.A. Hossain, R.M. Dawson, Chemical synthesis and biological evaluation of an antimicrobial peptide gonococcal growth inhibitor, Amino Acids 43 (2012) 2279–2283;
(d) M.A. Hossain, S. Matsumura, T. Kanai, K. Hamasaki, H. Mihara, A. Ueno, Association of α-helix peptides that have γ-cyclodextrin and pyrene units in their

side chain, and induction of dissociation of the association dimer by external stimulant molecules, J. Chem. Soc., Perkin Trans. 2 (2000) 1527–1533;
(e) V.B. Nair, C.S. Samuel, F. Separovic, M.A. Hossain, J.D. Wade, Human relaxin-2: historical perspectives and role in cancer biology, Amino Acids 43 (2012) 1131–1140.

[33] (a) S. Zhang, R.A. Hughes, R.A.D. Bathgate, F. Shabanpoor, M.A. Hossain, F. Lin, B.V. Lierop, A.J. Robinson, J.D. Wade, Role of the intra-A-chain disulfide bond of insulin-like peptide 3 in binding and activation of its receptor, RXFP2, Peptides 31 (2010) 1730–1736;
(b) M. Kocan, M. Sarwar, S.Y. Ang, J. Xiao, J.J. Marugan, M.A. Hossain, C. Wang, D.S. Hutchinson, C.S. Samuel, A.I. Agoulnik, R.A.D. Bathgate, R.J. Summers, ML290 is a biased allosteric agonist at the relaxin receptor RXFP1, Sci. Rep. 7 (2017) 2968;
(c) M.A. Hossain, L. Guilhaudis, A. Sonnevend, S. Attoub, B.J.V. Lierop, A.J. Robinson, J.D. Wade, J.M. Conlon, Synthesis, conformational analysis and biological properties of a dicarba derivative of the antimicrobial peptide, brevinin-1BYa, Eur. Biophys. J. 40 (2011) 555–564;
(d) W. Li, M.A. Sani, E. Jamasbi, L. Otvos, M.A. Hossain, J.D. Wade, F. Separovic, Membrane interactions of proline-rich antimicrobial peptide, Chex1-Arg20, multimers, Biochim. Biophys. Acta 2016 (1858) 1236–1243.

[34] F. Dong, Z. Zhao, T. Xiong, Z. Ni, W. Zhang, Y. Sun, W.K. Ho, In situ construction of g-C_3N_4/g-C_3N_4 metal-free heterojunction for enhanced visible-light photocatalysis, ACS Appl. Mater. Interfaces 5 (21) (2013) 11392–11401.

[35] G. Mamba, A. Mishra, Graphitic carbon nitride (g-C_3N_4) nanocomposites: a new and exciting generation of visible light driven photocatalysts for environmental pollution remediation, Appl. Catal. 198 (2016) 347–377.

[36] G. Gogoi, S. Keene, A.S. Patra, T.K. Sahu, S. Ardo, M. Qureshi, Hybrid of g-C_3N_4 and MoS_2 integrated onto Cd0. 5Zn0. 5S: rational design with efficient charge transfer for enhanced photocatalytic activity, ACS Sustain. Chem. Eng. 6 (5) (2018) 6718–6729.

[37] M. Li, L. Zhang, X. Fan, M. Wu, Y. Du, M. Wang, J. Shi, Dual synergetic effects in MoS_2/pyridine-modified g-C_3N_4 composite for highly active and stable photocatalytic hydrogen evolution under visible light, Appl. Catal. 190 (2016) 36–43.

[38] W. Grochala, The generalized maximum hardness principle revisited and applied to solids (Part 2), Phys. Chem. Chem. Phys. 19 (46) (2017) 30984–31006.

[39] T. Trindade, P. O'Brien, N.L. Pickett, Nanocrystalline semiconductors: synthesis, properties, and perspectives, J. Mater. Chem. 13 (11) (2001) 3843–3858.

[40] X. Dai, Q. Meng, F. Zhang, Y. Zou, C.A. Di, D. Zhu, Electronic structure engineering in organic thermoelectric materials, J. Energy Chem. 62 (2021) 204–219.

[41] R.E. Vernon, Organising the metals and nonmetals, Found. Chem. 22 (2) (2020) 217–223.

[42] X. Xiangrong, Encyclopedia of China: Mining and metallurgy china encyclopedia publishing house, (1998).

[43] C. Zhiming, Introduction to semiconductors publishing house of electronics industry, (2008).

[44] J. Tan, Z. Li, J. Li, J. Wu, X. Yao, T. Zhang, Graphitic carbon nitride-based materials in activating persulfate for aqueous organic pollutants degradation: a review on materials design and mechanisms, Chemosphere 262 (2021) 127675.

[45] A.K. Wahab, S. Ould-Chikh, K. Meyer, H. Idriss, On the "possible" synergism of the different phases of TiO_2 in photo-catalysis for hydrogen production, J. Catal. 352 (2017) 657–671.

[46] D. Chen, B. Li, Q. Pu, X. Chen, G. Wen, Z. Li, Preparation of Ag-$AgVO_3$/g-C_3N_4 composite photo-catalyst and degradation characteristics of antibiotics, J. Hazard. Mater. 373 (2019) 303–312.

[47] L. Ge, C. Han, X. Xiao, L. Guo, Synthesis and characterization of composite visible light active photocatalysts MoS_2–g-C_3N_4 with enhanced hydrogen evolution activity, Int. J. Hydrog. Energy 38 (17) (2013) 6960–6969.

[48] W. Qiu, S. Xiao, Y. Tong, S. Yang, Toward efficient charge collection and light absorption: a perspective of light trapping for advanced photoelectrodes, J. Phys. Chem. 123 (31) (2019) 18753–18770.